AIAA JOURNAL
Vol. 43, No. 10, October 2005

Space–Time Mapping Analysis of Airfoil Nonlinear Interaction with Unsteady Inviscid Flow

Vladimir V. Golubev* and Reda R. Mankbadi†
Embry–Riddle Aeronautical University, Daytona Beach, Florida 32114
and
Ray Hixon‡
Hixon Technologies, LLC, Fairview Park, Ohio 44126

A new computational method of space–time mapping analysis is applied to nonlinear, inviscid computation of unsteady airfoil response to an upstream flow with a finite amplitude of a time-harmonic vortical perturbation. The unique feature of the method is that it solves the unsteady problem as a steady-state one, by treating the time coordinate identically to space directions. The periodic nature of the flow is used to design the mesh covering one period of the vortical gust in the time direction, with a periodic boundary condition applied at the time-inflow and time-outflow boundaries. The computed solution is, thus, driven directly to the final long-time periodic solution using a pseudotime marching with a high-order discretization scheme. Computed unsteady aerodynamic and aeroacoustic airfoil responses are compared against available numerical solutions. Results obtained for a high-amplitude impinging gust identify zones in the computational domain where nonlinear response effects appear most significant.

Nomenclature

A	=	amplitude of perturbation velocity harmonic
E	=	total energy
$\boldsymbol{F}, \boldsymbol{G}$	=	inviscid flux vectors
J	=	mesh Jacobian
k	=	gust reduced frequency
$\boldsymbol{k}$	=	wave number vector
M	=	Mach number
N_x, N_y, N_t	=	space–time mesh dimensions
p	=	static pressure
$\boldsymbol{Q}$	=	vector of conservative flow variables
Re	=	real part
t	=	time
u, v	=	Cartesian velocity components
u_{BC}	=	velocity of outgoing perturbation
u_{boundary}	=	flow velocity at the inflow/outflow boundaries
$u_{\text{gust}}, v_{\text{gust}}$	=	gust velocity components
u'	=	perturbation flow velocity
$\bar{u}, \bar{v}, \bar{p}, \bar{\rho}$	=	mean flow variables
x, y	=	Cartesian space coordinates
α, β	=	gust wave numbers
γ	=	specific heats ratio
ε	=	gust intensity
ξ, η, τ	=	curvilinear space–time coordinates
ρ	=	density
ω	=	perturbation frequency

Presented as Paper 2004-3003 at the AIAA/CEAS 10th Aeroacoustics Conference, Manchester, England, United Kingdom, 10–13 May 2004; received 2 August 2004; revision received 11 April 2005; accepted for publication 28 April 2005.

*Associate Professor, Department of Aerospace Engineering, 600 South Clyde Morris. Senior Member AIAA.
†Professor, Department of Aerospace Engineering, 600 South Clyde Morris. Associate Fellow AIAA.
‡President. Member AIAA.

Introduction

In this work, we examine a recently developed numerical approach[1] referred to as the space–time mapping analysis (STMA) method, wherein a two- or three-dimensional unsteady problem is treated as a steady-state one in the three- or four-dimensional space–time. The approach was developed with the idea to extend high-accuracy discretization schemes developed in computational aeroacoustics (CAA) for spatial derivatives, to the time derivative, thus achieving highly time-accurate computations with absolute stability. Moreover, in terms of the distributed-memory parallel processing, the method appears to provide additional flexibility of clustering space–time grids in regions of rapid solution changes.

The problem of unsteady gust–airfoil interaction,[2] examined in the current paper, provides a convenient benchmark to investigate some of the beneficial features of the STMA method. For example, traditional CAA methods were developed to capture the transient behavior of an unsteady flow by combining a high-accuracy spatial differencing scheme with a time-marching method, thus, treating any unsteady problem as a transient problem and maintaining high time accuracy throughout the calculation process. On the other hand, the gust–airfoil interaction problem is an example of a periodic problem where the exact transient solution starting from the initial conditions may not be of interest. Instead, the long-term periodic solution is usually the desired output, with the excessive accuracy of the transient calculations being redundant. Thus, in the STMA approach, an unsteady marching problem in two spatial dimensions is transformed into a steady-state iterative problem in three dimensions. In the process, highly convergent iterative schemes from classical computational fluid dynamics can be applied, with a potential for increased computational accuracy by using better time derivatives, reduced CPU time because of less grid points in space–time and more efficient iterative methods, and improved parallel performance through larger block volumes on each processor and reduced synchronization needs during the iterative process.

Note that for general nonperiodic unsteady flows the STMA method can be applied by decomposing the total space–time computational domain into a series of blocks aligned in the time direction. In such arrangement, each block will have time-inflow and time-outflow boundaries, with the preceding block setting the time-inflow boundary for the current block and the current block setting the time-inflow boundary for the next block. A solution can be obtained by solving for each time–space block in sequence, thus imposing no restrictions on the space–time grid topology in the interior of each

block and allowing for an arbitrary clustering of grid points in the space–time areas of rapid solution changes. (Note that, in this approach, the time-inflow boundary is equivalent to a specified supersonic inflow boundary, whereas the time-outflow boundary is equivalent to an unspecified supersonic outflow boundary.) This ability is particularly important for unsteady problems with a wide range of length scales and time-scales, for example, rotor–stator interactions, where, for highly complex unsteady geometries, the STMA method can apply high-accuracy spatial differencing schemes without interpolation.

The paper first provides a review of governing equations for the gust–airfoil interaction problem, followed by a detailed account of issues in numerical formulation and implementation of the STMA method. Presented results and discussion are split in two parts. First, unsteady response solutions, computed for three frequencies of a small-amplitude impinging gust, are compared and validated against results obtained for the same cases in Refs. 3–5. Next, the analysis focuses on a single frequency, but variable amplitude of the gust, to examine the nonlinear response features.

Governing Equations

The current analysis of the gust–airfoil interaction problem is based on the numerical solution to nonlinear Euler equations, written in the Cartesian coordinates as

$$\boldsymbol{Q}_t + \boldsymbol{F}_x + \boldsymbol{G}_y = 0, \qquad \boldsymbol{Q} = \begin{bmatrix} \rho \\ \rho u \\ \rho v \\ E \end{bmatrix}$$

$$\boldsymbol{F} = \begin{bmatrix} \rho u \\ \rho u^2 + p \\ \rho uv \\ u(E+p) \end{bmatrix}, \qquad \boldsymbol{G} = \begin{bmatrix} \rho v \\ \rho uv \\ \rho v^2 + p \\ v(E+p) \end{bmatrix} \tag{1}$$

with the unsteady pressure calculated from

$$p = (\gamma - 1)\left(E - \tfrac{1}{2}\rho(u^2 + v^2)\right) \tag{2}$$

In this work, the gust response is investigated for a cambered, thick Joukowksi airfoil, which requires recasting the equations in the generalized curvilinear coordinates. In the traditional time-marching approach, implemented, for example, in Refs. 3 and 4, the employed transformation takes the form

$$\xi = \xi(x, y), \qquad \eta = \eta(x, y)$$

and the resulting Euler equations can be written as

$$\boldsymbol{Q}_t + \xi_x \boldsymbol{F}_\xi + \eta_x \boldsymbol{F}_\eta + \xi_y \boldsymbol{G}_\xi + \eta_y \boldsymbol{G}_\eta = 0 \tag{3}$$

However, in the STMA process, the governing equations (1) should be transformed into curvilinear coordinates that are all functions of space and time, as follows:

$$\xi = \xi(x, y, t), \qquad \eta = \eta(x, y, t), \qquad \tau = \tau(x, y, t) \tag{4}$$

When substituted into Eq. (1), the following equations are obtained in the strong conservation form:

$$[\tau_t(\boldsymbol{Q}/J) + \tau_x(\boldsymbol{F}/J) + \tau_y(\boldsymbol{G}/J)]_\tau + [\xi_t(\boldsymbol{Q}/J) + \xi_x(\boldsymbol{F}/J) + \xi_y(\boldsymbol{G}/J)]_\xi + [\eta_t(\boldsymbol{Q}/J) + \eta_x(\boldsymbol{F}/J) + \eta_y(\boldsymbol{G}/J)]_\eta = 0 \tag{5}$$

Note that the τ coordinate is defined in space–time in this approach, $\tau = \tau(x, y, t)$, rather than the usual definition of $\tau = \tau(t)$. Thus, there is no time variable in the STMA approach, and a standard time-marching approach cannot be used. Instead, an iterative method can be used to solve Eq. (5). In application to the unsteady gust–airfoil interaction problem, the periodic nature of the flow may be used to minimize the computational time and effort required to solve the test cases. Particularly, the mesh is designed to cover one period of the vortical gust in the time direction, with a periodic boundary condition applied at the time-inflow and time-outflow boundaries. Thus, the computed solution is driven directly to the final long-time periodic solution of interest, rather than expending effort in accurately resolving the initial transient solution.

Gust–Airfoil Interaction Model

In application to the gust–airfoil interaction problem, it can be assumed that the unsteadiness of the incident flow is superimposed far upstream on the mean flow in the form of the vortical, convected perturbation velocity, represented in the space of perturbation frequencies ω and wave number vectors $\boldsymbol{k}$ in the integral form

$$u'(\boldsymbol{x}, t) = \mathrm{Re}\left\{ \int_\omega \sum_k A_k(\boldsymbol{x}) \exp[i(\boldsymbol{k}\cdot\boldsymbol{x} - \omega t)] \right\} \tag{6}$$

The incident perturbation field is further considered to be of finite amplitude relative to the mean flow, to the level that one cannot assume a linear superposition of responses from each individual harmonic in Eq. (6). It is clear that, although the very notion of perturbation may become less obvious, the approach is valuable in that it allows to determine the limits of validity for the linear approach universally accepted in studies on unsteady aerodynamics and aeroacoustics. Thus, as in Refs. 2–5, the airfoil response is studied for the following distribution of the incident two-dimensional gust perturbation velocity:

$$u_{\text{gust}} = -\left(\varepsilon\beta M \Big/ \sqrt{\alpha^2 + \beta^2}\right)\cos(\alpha x + \beta y - \omega t)$$

$$v_{\text{gust}} = \left(\varepsilon\alpha M \Big/ \sqrt{\alpha^2 + \beta^2}\right)\cos(\alpha x + \beta y - \omega t) \tag{7}$$

where ε is the gust intensity relative to the mean flow and ω is the imposed gust frequency. The mean flow is defined far upstream from the airfoil as

$$\bar{\rho} = 1, \qquad \bar{u} = M, \qquad \bar{v} = 0, \qquad \bar{p} = (1/\gamma)(\bar{\rho}^\gamma) \tag{8}$$

where $\gamma = 1.4$. In the current study, the two-dimensional gust is considered with $\alpha = 2k$, $\beta = 2k$, and $\omega = 2kM$, where k is now the reduced frequency of the gust non-dimensionalized by the airfoil half-chord and the upstream mean flow velocity.

Numerical Implementation

The H2 Advanced Concepts, Inc., mapping analysis research code (MARC) has been developed to solve the STMA equations.[1] This solver uses the Tam and Webb[6] seven-point, 4th-order dispersion relation preserving scheme, with the 10th-order artificial dissipation[7] added in all coordinate directions. In application to the cases to be presented, this study uses a simple iterative procedure by adding a timelike term to solve Eq. (5). In the future, convergence acceleration techniques such as implicit residual smoothing, local time stepping, and multigrid methods may be added to improve greatly the computational efficiency of the code.

Figure 1 shows the three-dimensional computational domain (x, y, z), where $z = t$, along with contours of the computed conservative variable ρv from the solution vector $\boldsymbol{Q}$ in Eq. (1) obtained in a case study for the gust reduced frequency $k = 1.0$. Note that the time coordinate points in the z direction. The translucent contours, thus, show gust evolution both in space and time.

The (x, y) planes correspond to slices of the (x, y, t) domain, with the airfoil located in middle of the plane (in Fig. 2). Note that the same (x, y) plane was used as the entire computational domain in Refs. 3 and 4, where the conventional time marching was applied. The C grid for the (x, y) plane is generated as a single block around a thick, cambered Joukowski airfoil using GridPro® commercial grid-generation software.[8]

At the beginning of the iterative, pseudo-time-marching convergence process, the flow is initialized throughout the physical domain, with the gust perturbation superimposed on the mean flow.

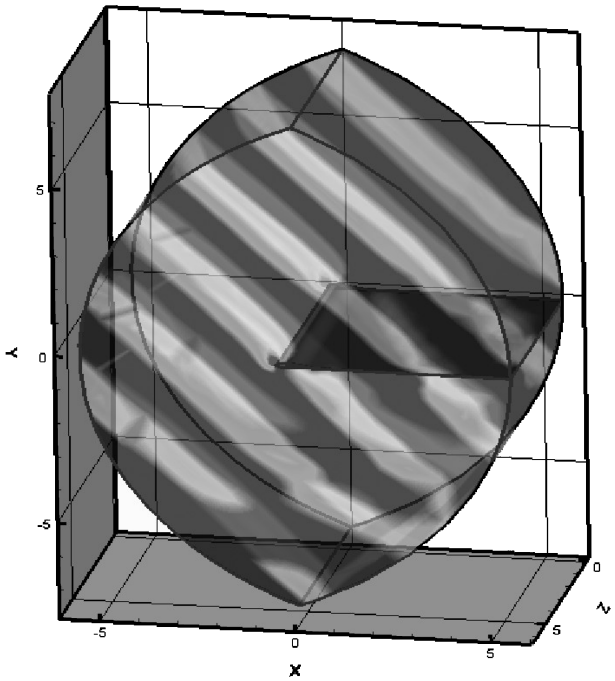

Fig. 1 Computational (x, y, t) domain with contours of instantaneous ρv component of gust, $k = 1.0$ and $\varepsilon = 0.2$.

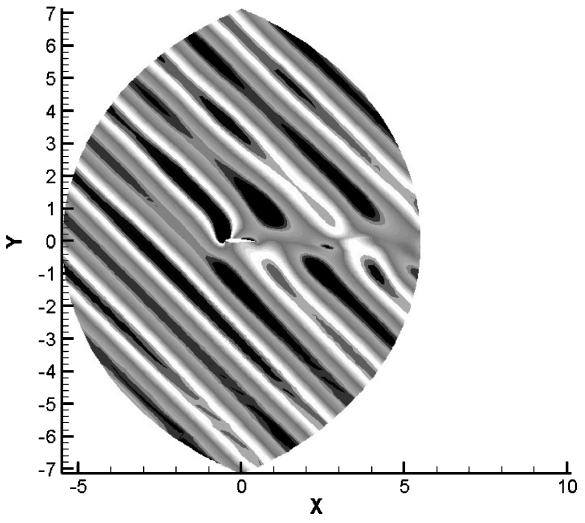

Fig. 2 Slice (x, y) of (x, y, t) domain in Fig. 1.

At the inflow boundary of each (x, y) plane, the standard acoustic radiation condition is applied to the outgoing perturbation, defined, for example, for the x component of the flow velocity as $u_{BC} = u_{\text{boundary}} - \bar{u} - u_{\text{gust}}$. At the outflow boundary of each (x, y) plane, Tam and Webb's[6] condition is applied.

In the current work, computations for three selected gust frequencies are run on three different meshes, corresponding to $N_x \times N_y \times N_t = (605 \times 240 \times 17)$, $(433 \times 125 \times 17)$, and $(433 \times 125 \times 33)$. The first two meshes are discretized with 17 points per one period of the gust in the time direction and are used in low-amplitude gust response calculations. The last grid is designed to cover two periods of the gust with 33 points in the time direction. It is employed in high-amplitude gust calculations to examine generation of higher frequency harmonics in the nonlinear airfoil response.

The current status of the code only allows for computations on a single processor, which requires a significant computer memory. A typical case run on a 2.8-GHz, 2-GB SDRAM Intel-4 processor was taking up to two weeks to fully converge on the finest mesh.

Results and Discussion

The computations discussed in this paper were conducted for gust reduced frequencies $k = 0.1$, 1.0, and 2.0. The unsteady response was investigated for a loaded, 12% thick, 2% cambered Joukowski airfoil at a 2-deg angle of attack. In all computations, Mach number was fixed at $M = 0.5$.

Results for low-amplitude gust response, calculated for all three frequencies, are examined first. These solutions are compared and validated against results obtained for similar cases in Refs. 3–5. The analysis then focuses on a single gust frequency of $k = 1.0$ and examines the nonlinear response features for gust intensities ranging from $\varepsilon = 0.02$ to $\varepsilon = 0.4$.

Low-Amplitude Gust Response for $k = 0.1$, 1.0, and 2.0

The STMA results obtained for the gust amplitude of $\varepsilon = 0.02$ are shown in Figs. 3–12. The mean pressure distribution on the airfoil surface is practically identical for all gust frequencies and compares well with FLO36 mean flow solver[9] predictions in Fig. 3. (The latter is employed in GUST3D code[10,11] to compute the mean flow input.)

In Figs. 4–6, the predicted airfoil surface rms unsteady pressure is compared against GUST3D results,[5] as well as solutions computed in Refs. 3 and 4. Note that the latter match closely with results predicted by the MARC code, whereas GUST3D results start to show deviation from both time-accurate solutions at $k = 2.0$. This could be related to the known loss of accuracy in GUST3D at higher reduced frequencies, usually more pronounced in the far-field predictions as will be mentioned subsequently. Relatively minor wiggles at the trailing edge in the STMA solutions (in Figs. 5 and 6) are attributed to the effect of the employed C-grid topology. (At the trailing edge,

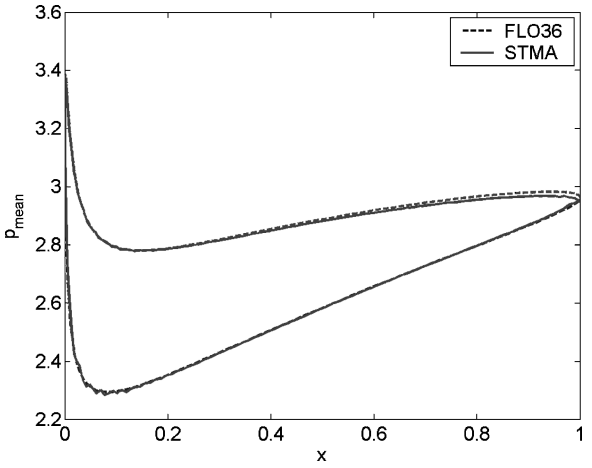

Fig. 3 Mean pressure on airfoil surface: comparison of FLO36 solution with STMA prediction.

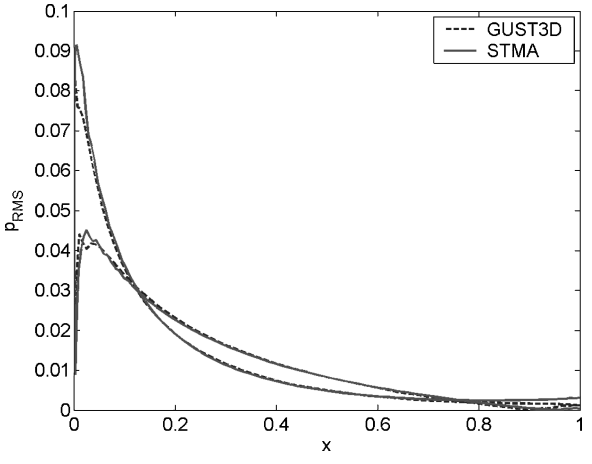

Fig. 4 RMS pressure on airfoil surface, $k = 0.1$ and $\varepsilon = 0.02$.

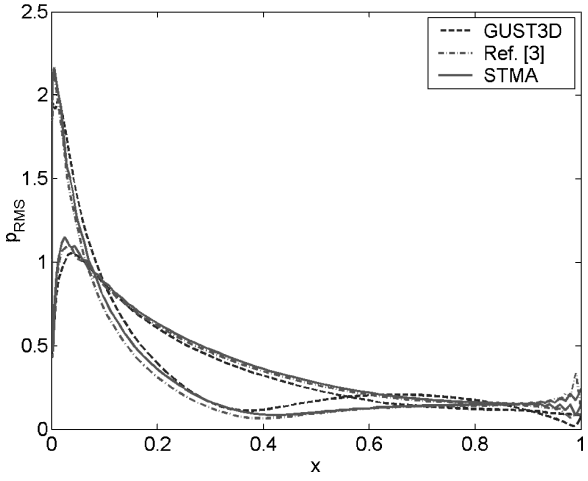

Fig. 5 RMS pressure on airfoil surface, $k = 1.0$ and $\varepsilon = 0.02$.

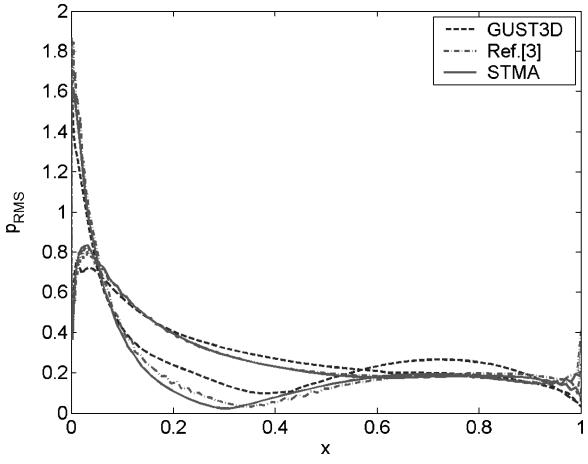

Fig. 6 RMS pressure on airfoil surface, $k = 2.0$ and $\varepsilon = 0.02$.

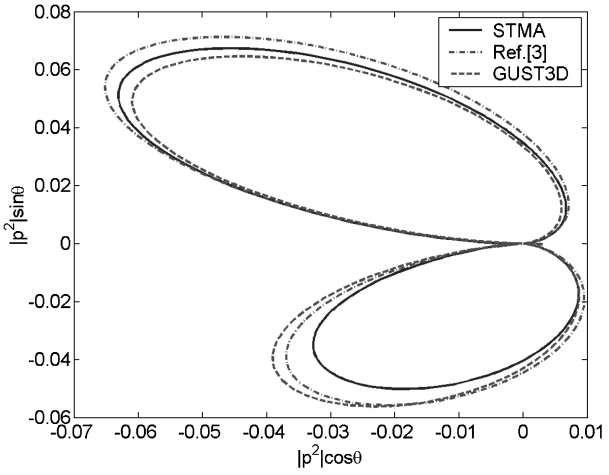

Fig. 7 Distribution of $|p'^2|$ at $R = 1$, $k = 0.1$ and $\varepsilon = 0.02$.

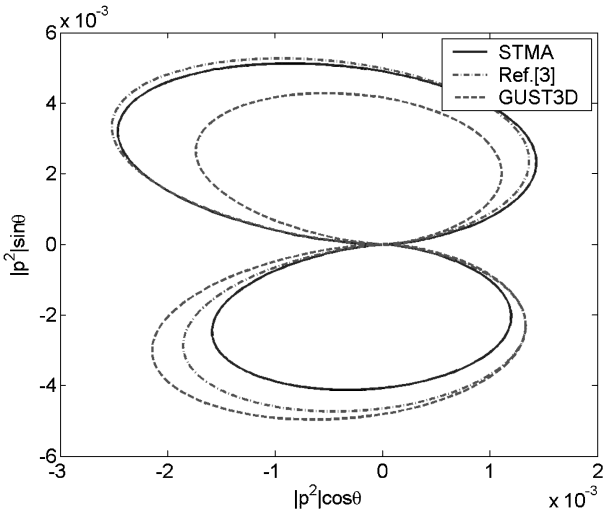

Fig. 8 Distribution of $|p'^2|$ at $R = 4$, $k = 0.1$ and $\varepsilon = 0.02$.

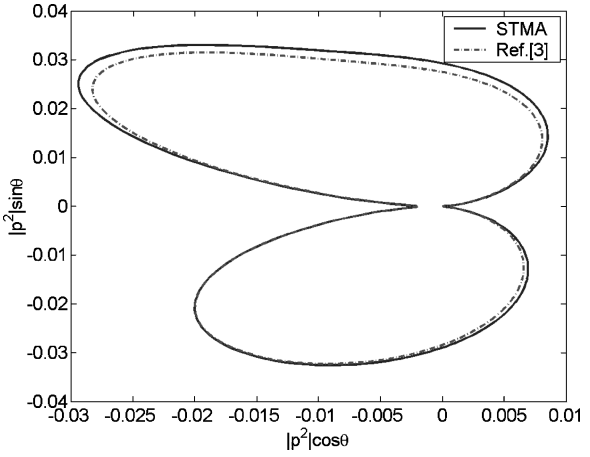

Fig. 9 Distribution of $|p'^2|$ at $R = 1$, $k = 1.0$ and $\varepsilon = 0.02$.

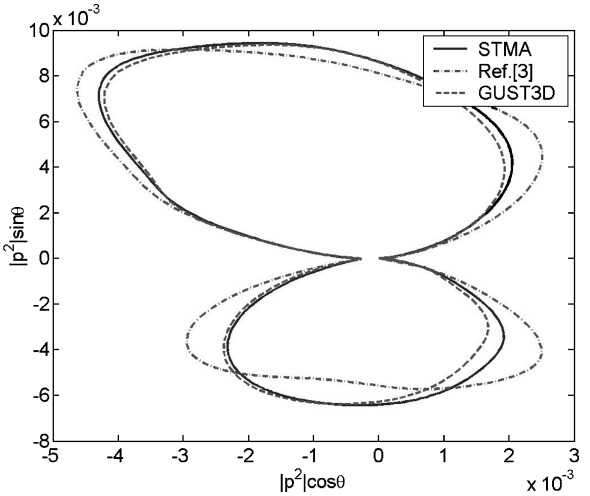

Fig. 10 Distribution of $|p'^2|$ at $R = 4$, $k = 1.0$ and $\varepsilon = 0.02$.

the grid line that defines the wall comes off the airfoil and extends down the wake cut. When using a high-order scheme, the transition from the airfoil wall boundary to the connection across the wake is seen by the code as a discontinuity, thus resulting in characteristic wiggles.) This choice, in turn, is dictated by the need to set properly the Kutta condition for the code. (Normally, an Euler code sets the Kutta condition via the artificial dissipation. However, the MARC code has such a low dissipation that the C-grid is necessary to force the flow to separate from the trailing edge.)

The directivity for the nondimensional acoustic intensities is shown in Figs. 7–12, for each frequency calculated at distances $R = 1$ and 4 from the airfoil centerpoint (everywhere normalized by the airfoil chord). For $k = 0.1$, STMA results show good comparison with other codes for the upper lobe but slightly underpredict those for the lower lobe. The recently improved GUST3D version[11] provided with almost identical far-field solution at $k = 1.0$, whereas a good agreement with results from Refs. 3 and 4 is noted in the near field, $R = 1$. Deviations with the latter in the far-field predictions may be

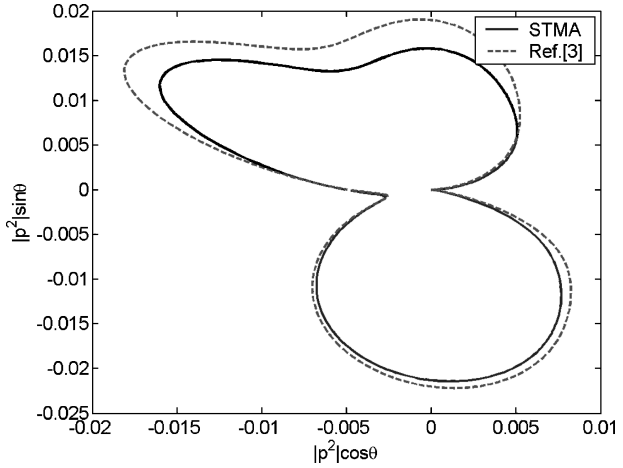

Fig. 11 Distribution of $|p'^2|$ at $R = 1$, $k = 2.0$ and $\varepsilon = 0.02$.

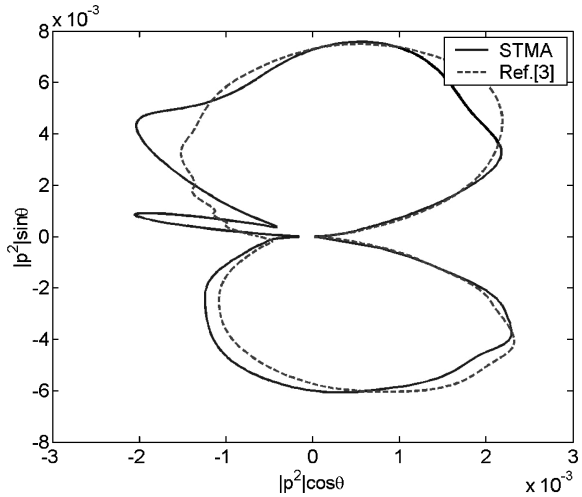

Fig. 12 Distribution of $|p'^2|$ at $R = 4$, $k = 2.0$ and $\varepsilon = 0.02$.

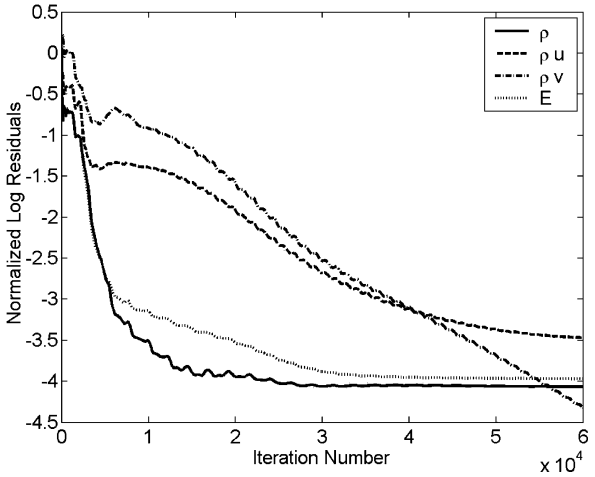

Fig. 13 Normalized logarithm of L^2-norm solution residuals vs iteration step of pseudo-time marching, $k = 2.0$ and $\varepsilon = 0.2$, 433 × 125 × 17 mesh.

attributed to certain far-field boundary reflection problems reported in Ref. 3. Finally, note that at $k = 2.0$, the STMA-predicted far-field directivity, $R = 4$, starts to exhibit some distortions in the lobes. On the other hand, this result was obtained on the 605 × 240 × 17 grid, the finest used in the current computations because of the computer memory limitations. (The lower frequency cases employed the 433 × 125 × 17 mesh.) In Ref. 4, reasonable far-field solutions for this frequency on such a mesh were not achieved due to a poor gust resolution (providing only about 8 points per wavelength), and the Ref. 3 result, shown for comparison in Fig. 12, was obtained only after employing a finer 515 × 971 mesh. (Refer to Ref. 3 for more discussion on the issue of grid resolution.) Note that for $k = 2.0$, no stable solution was obtained in GUST3D calculations.

High-Amplitude Gust Response for $k = 1.0$

We now examine results for the airfoil unsteady response obtained at various amplitudes of the incident gust (ranging from $\varepsilon = 0.02$ to

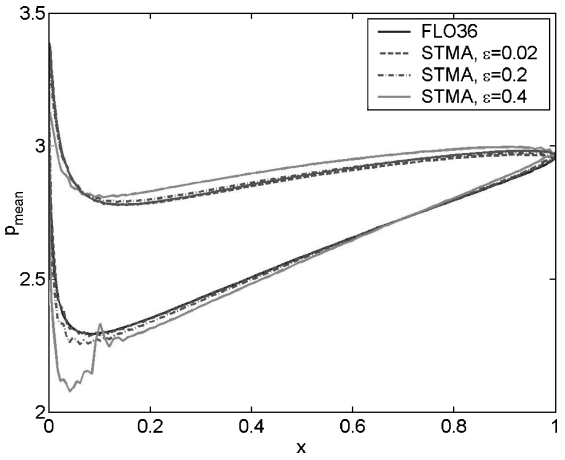

Fig. 14 Mean pressure on surface: comparison of FLO36 solution with STMA predictions at $\varepsilon = 0.02$, 0.2, and 0.4.

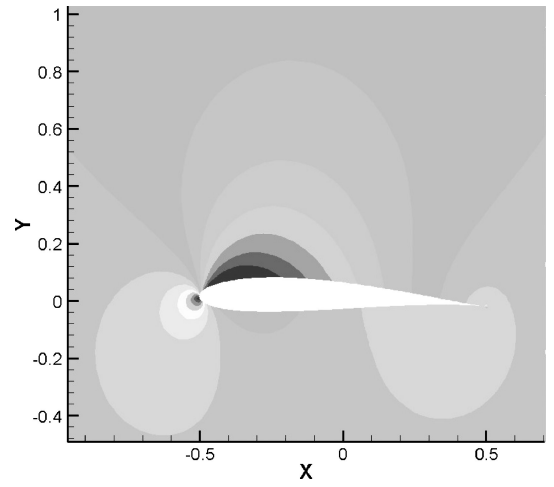

Fig. 15 Mean pressure contours for $\varepsilon = 0.02$ (STMA calculation).

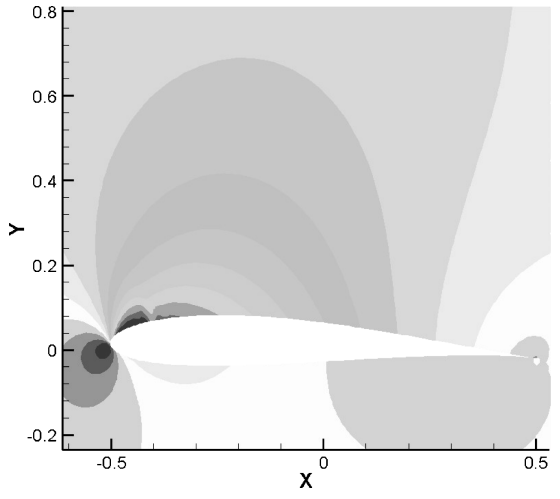

Fig. 16 Mean pressure contours for $\varepsilon = 0.4$ (STMA calculation).

$\varepsilon = 0.4$), for the gust reduced frequency $k = 1.0$. A typical convergence plot for L^2-norm solution residuals, obtained for $\varepsilon = 0.2$ case after 60,000 pseudo-time-marching steps on the $433 \times 125 \times 17$ mesh, is shown in Fig. 13.

Note that, along the airfoil surface, the aerodynamic response contains both the mean (due to the airfoil camber and angle of attack) and unsteady perturbation (due to the incident gust) pressure components. The results for the mean pressure distribution on the suction and pressure sides, computed for different gust amplitudes, are compared in Fig. 14 with computations from FLO36 mean flow solver.[9] Note that the STMA results are generally in good agreement with FLO36 solution, with a sharp deviation observed near the leading edge for the highest gust intensity of $\varepsilon = 0.4$. In fact, the STMA-predicted pressure contours in Figs. 15 and 16 for $\varepsilon = 0.02$ and 0.4, respectively, show the presence of a shock and a small supersonic bubble in the case of the maximum gust amplitude. This produces characteristic wiggles observed in Fig. 14 near the shock region. The following fast Fourier transform (FFT) analysis of the pressure solution will, in fact, indicate the character of the energy transfer between the mean flow and the higher frequency harmonics in this case.

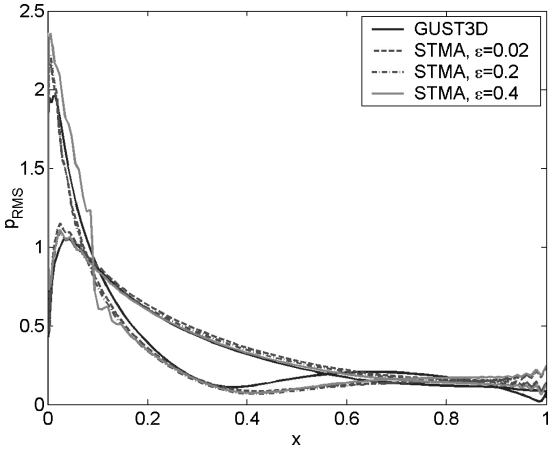

Fig. 17 RMS pressure on airfoil surface: comparison of GUST3D solution with STMA predictions at $\varepsilon = 0.02$, 0.2, and 0.4.

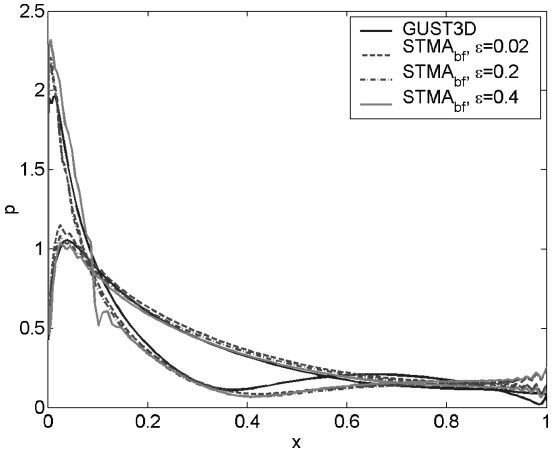

Fig. 18 Base harmonic of pressure FFT on airfoil surface: comparison of GUST3D rms solution with STMA predictions at $\varepsilon = 0.02$, 0.2, and 0.4.

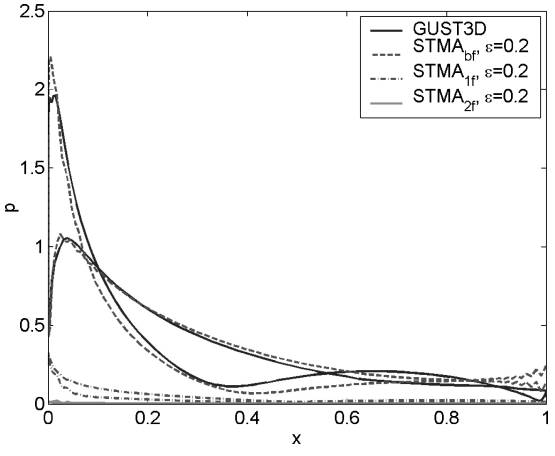

Fig. 19 Base, first, and second harmonics of pressure FFT on airfoil surface: comparison of GUST3D rms solution with STMA predictions at $\varepsilon = 0.2$.

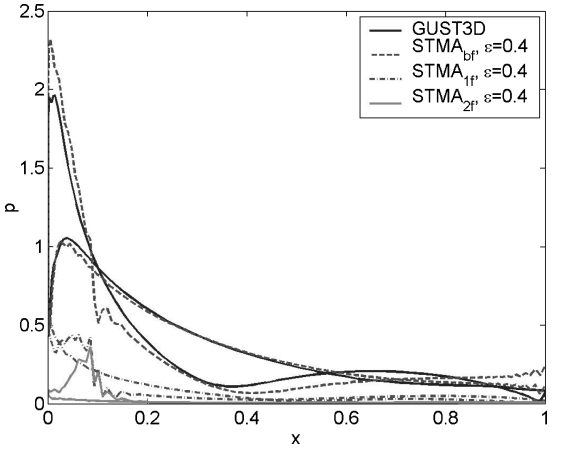

Fig. 20 Base, first, and second harmonics of pressure FFT on airfoil surface: comparison of GUST3D rms solution with STMA predictions at $\varepsilon = 0.4$.

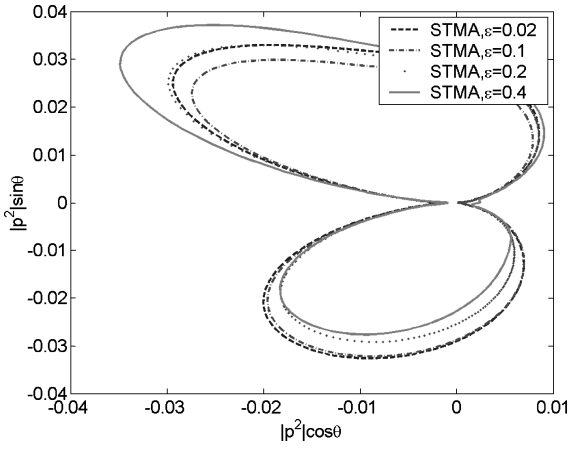

Fig. 21 Directivity of $|p'^2|$ for rms pressure at $R = 1$.

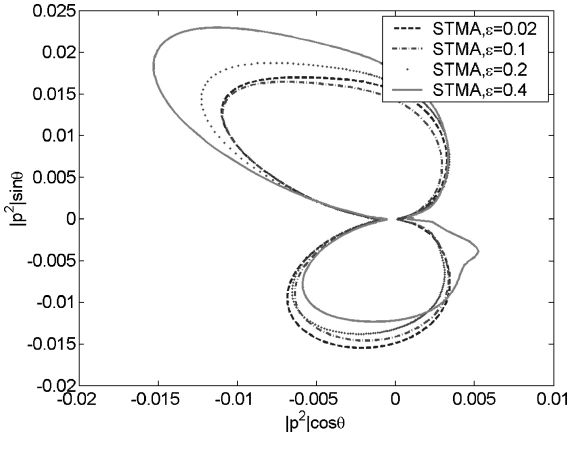

Fig. 22 Directivity of $|p'^2|$ for rms pressure at $R = 2$.

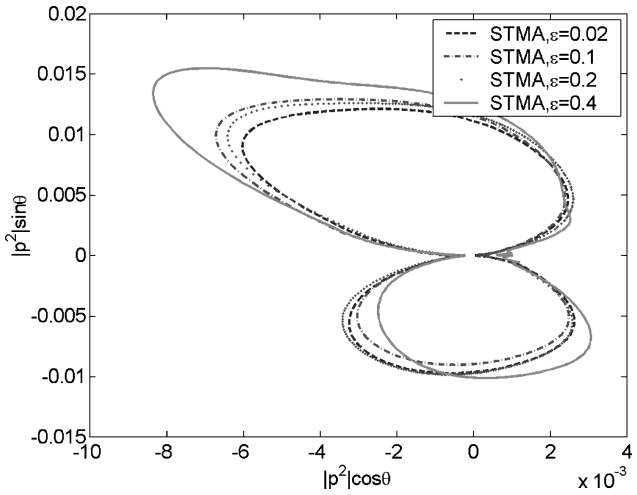

Fig. 23 Directivity of $|p'^2|$ for rms pressure at $R = 3$.

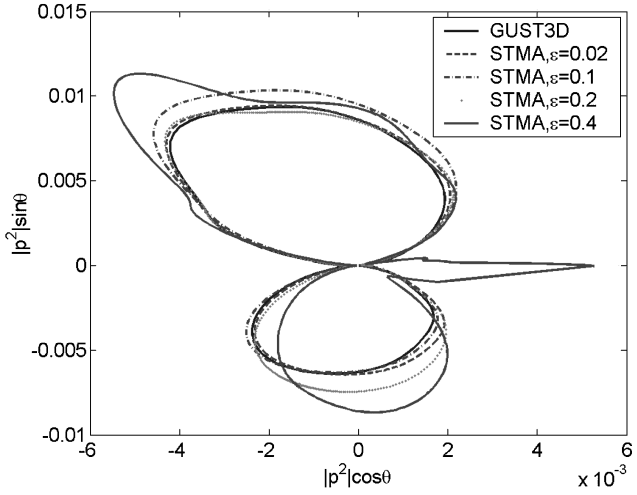

Fig. 24 Directivity of $|p'^2|$ for rms pressure at $R = 4$.

Figures 17–20 focus on the airfoil unsteady pressure RMS solutions and their FFT analysis. A general comparison of GUST3D rms pressure predictions with STMA computations for different gust intensities is provided in Fig. 17. The response amplitudes are scaled to the same input gust amplitude to allow proper comparison. In all cases, the agreement is excellent between STMA and GUST3D solutions, with small deviations observed near the trailing edge due to a local loss of numerical accuracy. Interestingly enough, the earlier observed significant deviation in the mean pressure near the leading edge for $\varepsilon = 0.4$ does not propagate into much larger deviation in the overall unsteady rms pressure response from the GUST3D prediction in Fig. 17. For all gust amplitudes, the base FFT harmonics of the airfoil pressure responses appear close to GUST3D predictions in Fig. 18, except for a localized wiggle at $x = 0.1$ in the case of the highest gust amplitude. Figures 19 and 20 provide further explanation of the nonlinear response by showing the first three FFT harmonics of the unsteady STMA solution for $\varepsilon = 0.2$ and 0.4. Note that, for $\varepsilon = 0.4$, both higher harmonics show a significant presence in the shock region (approaching $x = 0.1$), thus, confirming the importance of nonlinear effects in this area. It also appears that the nonlinear energy transfer from the mean flow is spread between all harmonics in Fig. 20 in such a way that the overall unsteady rms pressure remains rather close to the linear response predictions in Fig. 17. (A certain resulting elevation in the amplitude of the rms response near the leading edge still may be noted.) Overall, apart from the noticeable shock effects at $\varepsilon = 0.4$, no significant nonlinear impact on the unsteady aerodynamic response is noted with increasing gust amplitudes.

The unsteady pressure predictions in the near to far fields surrounding the airfoil are shown in terms of the directivity contours for the predicted intensity of the unsteady pressure signal. Results shown in Figs. 21–24 provide the directivity at radii $R = 1$, 2, 3, and 4, respectively. As before, the unsteady responses are scaled to the same input gust amplitude. The obtained solutions thus indicate the nonlinear effect of the increasing gust amplitudes on the airfoil near-field and far-field acoustic responses.

To better understand the nature of the amplitude changes and distortions in the directivity observed in Figs. 21–24 and particularly noticeable for $\varepsilon = 0.4$, the directivity contours were also calculated for the base and first FFT harmonics of the unsteady pressure signal.

As clearly observed in Figs. 25 and 26, the nonlinear effects do increase significantly for $\varepsilon = 0.4$, compared to lower gust intensities.

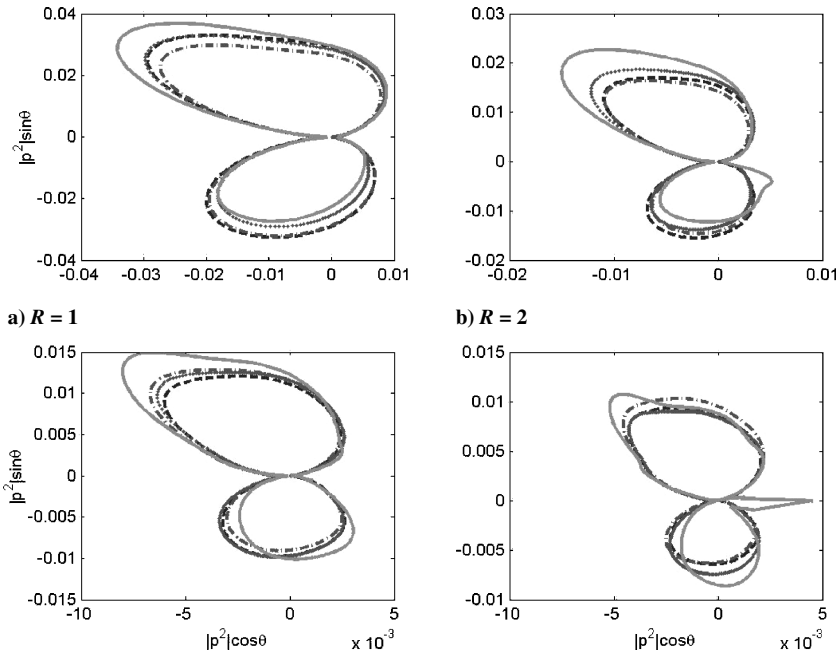

a) $R = 1$ **b) $R = 2$**

c) $R = 3$ **d) $R = 4$**

Fig. 25 Directivities of $|p'^2|$ for base FFT harmonic at $R = 1$, 2, 3, and 4.

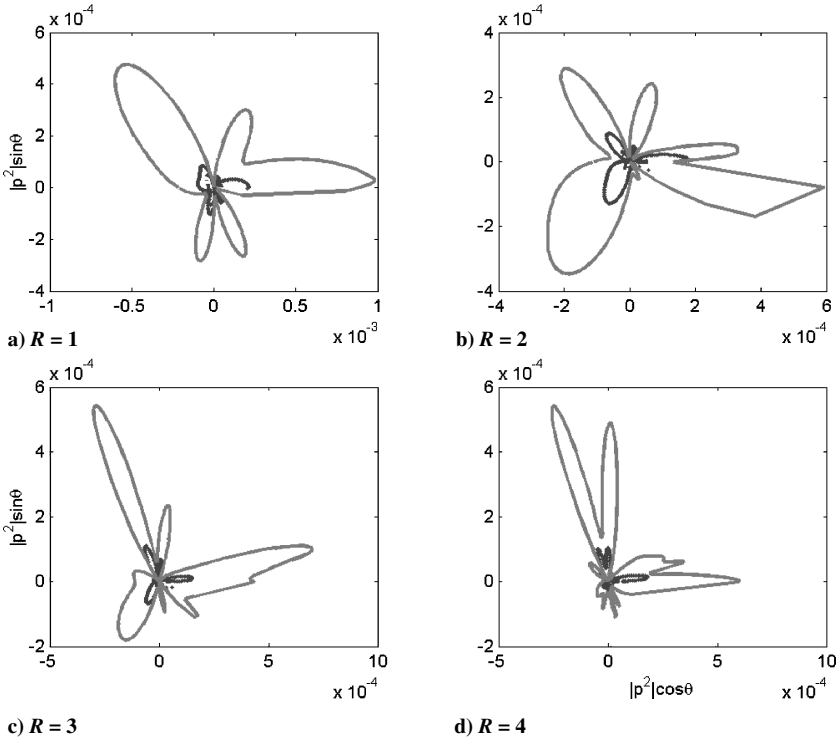

Fig. 26 Directivities of $|p'^2|$ for first FFT harmonic at $R = 1$, 2, 3, and 4.

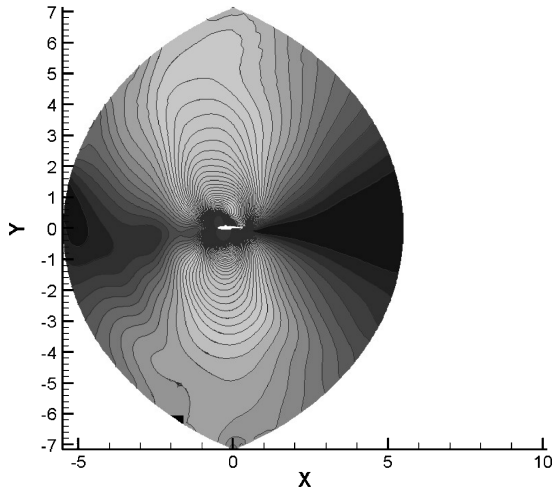

Fig. 27 RMS of unsteady pressure for $\varepsilon = 0.02$.

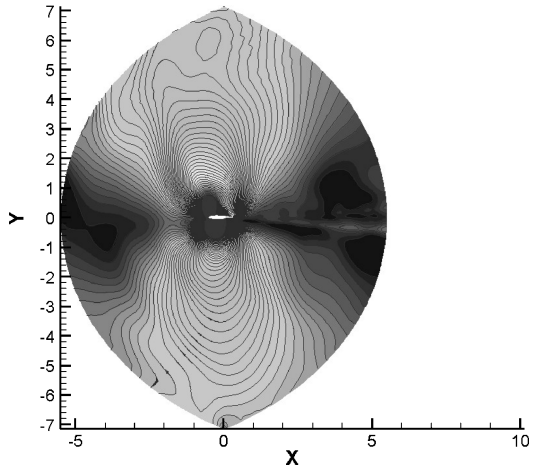

Fig. 28 RMS of unsteady pressure for $\varepsilon = 0.2$.

As will be further demonstrated, the nonlinear wake instability, while enhancing with higher gust amplitudes, gives rise to the axial spike in Fig. 25d, which is actually a result of the hydrodynamic pressure from the large wake vortex located at $R = 4$. At the same time, note that the first harmonic remains one to two orders of magnitude lower than the base harmonic, and the latter shows the same distortion of the upper lobe in Fig. 25d observed for rms pressure in Fig. 24. The first harmonic appears to extend in the same direction of the lobe distortion (in Fig. 26d), which nonlinear effect, thus includes generation of higher harmonics. In general, the observed distortion in the lobe pattern could point to the appearance of a noncompact acoustic source, for example, due to the shock presence. To obtain a clearer picture and to quantify these phenomena, the contour plots of the unsteady rms pressure and FFT harmonics are presented next.

Qualitative Analysis of Nonlinear Response

To further understand the qualitative behavior of the unsteady solution throughout the domain, the unsteady pressure contour plots are now examined.

For comparison, the linear response for $\varepsilon = 0.02$ is shown in Fig. 27. The contours illustrate propagation of the acoustics away from the airfoil, along with the formation of the characteristic dipole-type radiation pattern observed in the earlier directivity plots.

Whereas Fig. 27 contains no (at least apparent) indication of the nonlinear wake development, both the cases of $\varepsilon = 0.2$ and 0.4 (in Figs. 28 and 29) show significant effects of the nonlinear wake evolution, accompanied by strong hydrodynamic pressure pulsations. Enlarged in Fig. 30 for $\varepsilon = 0.4$, this region shows characteristic vortex rollups and pairings, indicative of the nonlinear, inviscid wake instability. In general, an acoustic radiation pattern may develop from such nonlinear vortex interactions, but this is not evident from the current results.

The presence of higher harmonics of the unsteady pressure response is further confirmed by comparing the base and the first FFT harmonics in Figs. 31 and 32, for $\varepsilon = 0.4$. The nonlinearity, exhibited by the presence of the first pressure harmonic, is clearly localized in the wake region, but it is also seen in the direction where the directivity lobe has been observed to develop a significant distortion (in Fig. 24).

Finally, to quantify and localize effects from the nonlinear gust–airfoil interaction, the difference of the appropriately scaled (by the corresponding amplitudes, for a unit input) base frequency and rms of unsteady, linear pressure response are shown in Figs. 33–35 for $\varepsilon = 0.02$, 0.2, and 0.4. Note that zero difference in this case is an indication of a purely linear response. Interestingly enough, some evidence of wake nonlinearity appears present even at $\varepsilon = 0.02$, but the deviation from the linear behavior is very small (of the order

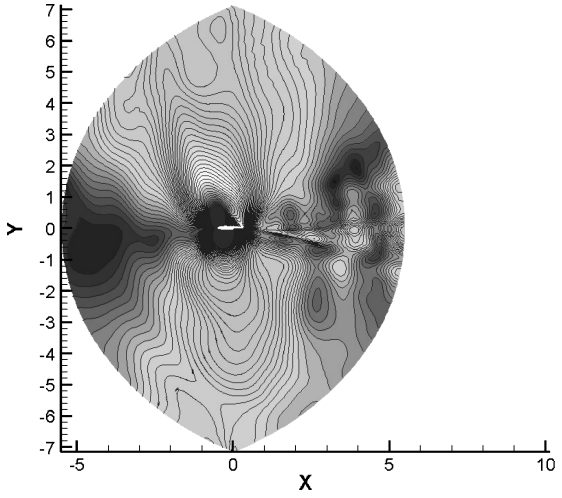

Fig. 29 RMS of unsteady pressure for $\varepsilon = 0.4$.

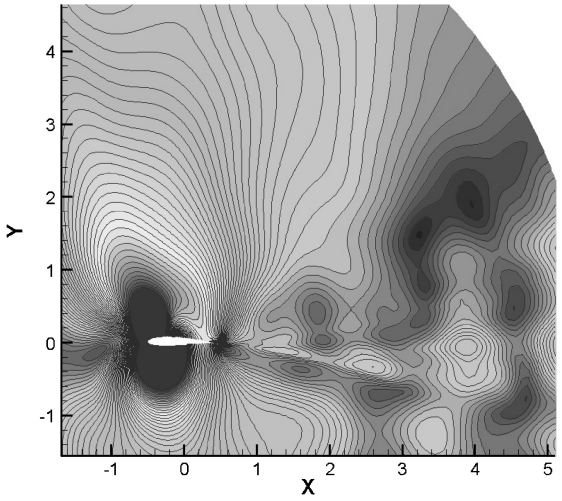

Fig. 30 RMS of unsteady pressure for $\varepsilon = 0.4$: airfoil and wake regions.

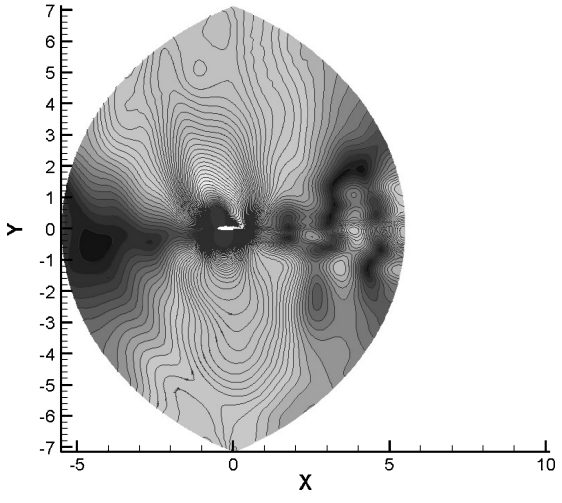

Fig. 31 FFT of unsteady pressure, base harmonic, $\varepsilon = 0.4$.

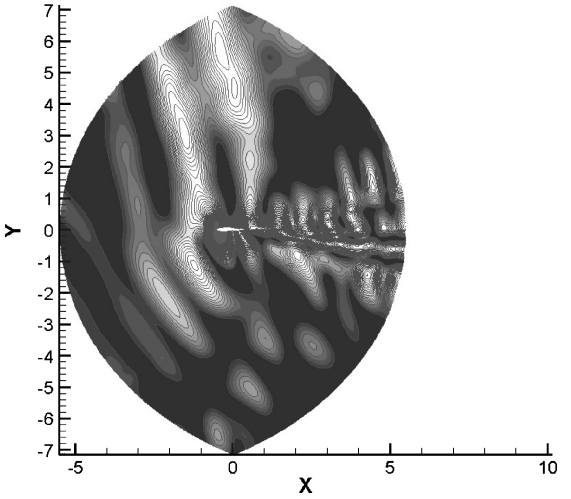

Fig. 32 FFT of unsteady pressure, first harmonic, $\varepsilon = 0.4$.

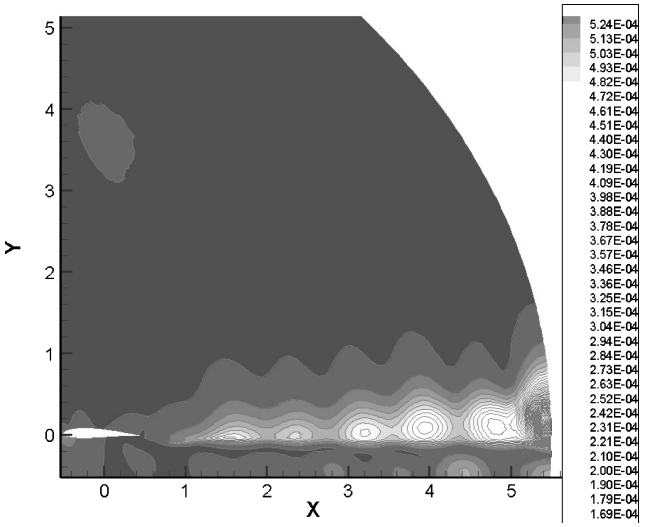

Fig. 33 Difference of base frequency and linear-response rms of unsteady pressure, $\varepsilon = 0.02$.

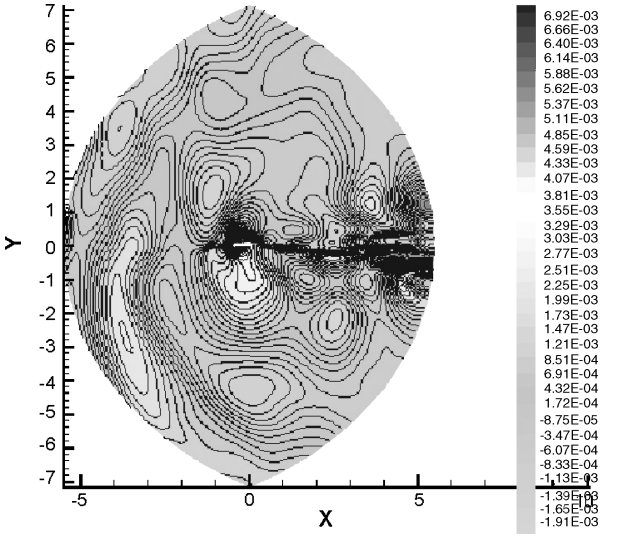

Fig. 34 Difference of base harmonic and linear-response rms of unsteady pressure, $\varepsilon = 0.2$.

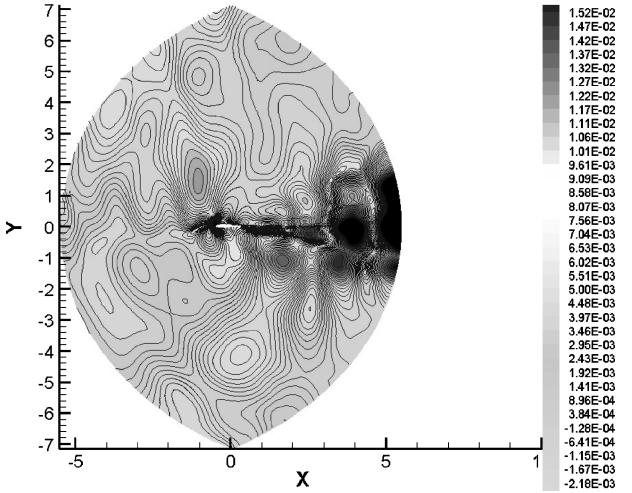

Fig. 35 Difference of base harmonic and linear-response rms of unsteady pressure, $\varepsilon = 0.4$.

of $1.e{-}4$). On the contrary, the nonlinearities are clearly present for higher gust intensities. Again, those are mostly localized in the wake, but are also seen in the region above the airfoil. The relative amplitude of these nonlinearities increases from about $1.e{-}3$ for $\varepsilon = 0.2$, to approximately $1.e{-}2$ for $\varepsilon = 0.4$, thus confirming the earlier observations.

Conclusions

Application of the STMA method to prediction of the nonlinear unsteady airfoil response to an impinging, finite-amplitude gust is examined. When the time coordinate is treated identically to the space directions, the STMA method essentially solved the unsteady two-dimensional interaction problem as a steady-state three-dimensional one. A high-order discretization scheme was applied to achieve time-accurate predictions of both unsteady aerodynamic and aeroacoustic responses.

The results for the two-dimensional small-amplitude gust interaction with a cambered, thick Joukowski airfoil at an angle of attack were calculated for the mean flow Mach number $M = 0.5$ and gust reduced frequencies $k = 0.1$, 1.0, and 2.0. For the case of $k = 1.0$, solutions for a high-intensity gust–airfoil interaction were obtained, for gust amplitudes ranging from $\varepsilon = 0.02$ to 0.4. To validate numerical computations, a comparison was conducted with the frequency-domain linear solver GUST3D and another time-marching solver. Excellent agreement was observed for the mean and rms pressure predictions along the airfoil surface between all solutions. The far-field acoustic directivities also compared well.

The results obtained from nonlinear high-amplitude gust calculations identified zones in the computational domain where nonlinear response effects appeared most significant. Such zones have been detected primarily in the wake region, but were also observed in the region above the airfoil.

Acknowledgment

The authors thank James R. Scott for providing GUST3D data and valuable comments.

References

[1]Hixon, R., "Space–Time Mapping Analysis for the Accurate Calculation of Complex Unsteady Flows," AIAA Paper 2003-3205, May 2003.

[2]Scott, J. R., "Sound Generation by Interacting with a Gust. Problem 1—Single Airfoil Gust Response," *Proceedings of the 4th CAA Workshop on Benchmark Problems*, NASA CP 2004-212954, Oct. 2003, pp. 13–17.

[3]Golubev, V. V., Mankbadi, R. R., and Scott, J. R., "Numerical Inviscid Analysis of Nonlinear Airfoil Response to Impinging High-Intensity High-Frequency Gust," AIAA Paper 2004-3002, May 2004.

[4]Golubev, V. V., Mankbadi, R. R., and Hixon, R., "Simulation of Airfoil Response to Impinging Gust Using High-Order Prefactored Compact Code,"*Proceedings of the 4th CAA Workshop on Benchmark Problems*, NASA CP 2004-212954, Oct. 2003, pp. 141–148.

[5]Scott, J. R., "Single Airfoil Gust Response Problem," *Proceedings of the 4th CAA Workshop on Benchmark Problems*, NASA CP 2004-212954, Oct. 2003, pp. 45–58.

[6]Tam, C. K. W., and Webb, J. C., "Dispersion-Relation-Preserving Finite-Difference Schemes for Computational Acoustics," *Journal of Computational Physics*, Vol. 107, No. 2, 1993, pp. 262–281.

[7]Kennedy, C. A., and Carpenter, M. H., "Several New Numerical Methods for Compressible Shear-Layer Simulations," *Applied Numerical Mathematics*, Vol. 14, No. 4, 1994, pp. 397–433.

[8]GridPro^{TM}, Program Development Corp., White Plains, NY, 2005.

[9]Jameson, A., and Caughey, D. A., "A Finite Volume Method for Transonic Potential Flow Calculations," *Proceedings of the 3rd AIAA Computational Fluid Dynamics Conference*, AIAA, New York, 1979, p. 122.

[10]Scott, J. R., and Atassi, H. M., "A Finite-Difference, Frequency-Domain Numerical Scheme for the Solution of the Gust-Response Problem," *Journal of Computational Physics*, Vol. 119, No. 1, 1995, pp. 75–93.

[11]Scott, J. R., Atassi, H. M., and Susan-Resiga, R. F., "A New Domain Decomposition Approach for the Gust Response Problem," AIAA Paper 2003-0883, Jan. 2003.

D. Gaitonde
Associate Editor